

RESEARCH

Open Access



# Experimental design for a novel co-flow jet airfoil

Hao Jiang<sup>1</sup>, Weigang Yao<sup>2\*</sup> and Min Xu<sup>1†</sup>

\*Weigang Yao and Min Xu contributed equally to this work.

\*Correspondence:  
weigang.yao@dmu.ac.uk

<sup>1</sup> School of Astronautics,  
Northwestern Polytechnical  
University, Xi'an 710072, China

<sup>2</sup> Faculty of Computing,  
Engineering and Media, De  
Montfort University, Leicester LE1  
9BH, UK

## Abstract

The Co-flow Jet (CFJ) technology holds significant promise for enhancing aerodynamic efficiency and furthering decarbonization in the evolving landscape of air transportation. The aim of this study is to empirically validate an optimized CFJ airfoil through low-speed wind tunnel experiments. The CFJ airfoil is structured in a tri-sectional design, consisting of one experimental segment and two stationary segments. A support rod penetrates the airfoil, fulfilling dual roles: it not only maintains the structural integrity of the overall model but also enables the direct measurement of aerodynamic forces on the test section of the CFJ airfoil within a two-dimensional wind tunnel. In parallel, the stationary segments are designed to effectively minimize the interference from the lateral tunnel walls. The experimental results are compared with numerical simulations, specifically focusing on aerodynamic parameters and flow field distribution. The findings reveal that the experimental framework employed is highly effective in characterizing the aerodynamic behavior of the CFJ airfoil, showing strong agreement with the simulation data.

**Keywords:** Co-flow jet, Wind tunnel experiment, Flow control, Wall effect

## 1 Introduction

The Co-flow Jet (CFJ) technology heralds a novel paradigm in active flow control [1–4], boasting superior aerodynamic properties. These characteristics position CFJ as a pivotal technological advancement, supporting the evolution of future aircraft towards lighter and more environmentally sustainable designs. Intricately, the CFJ system positions a compressor within the airfoil's architecture. It capitalizes on the principle of zero-net-mass flux [5] for controlling air circulation. This is achieved by introducing air at the leading edge and simultaneously extracting it at the trailing edge of the airfoil's upper surface [6, 7]. Such a mechanism augments lift, diminishes drag, and expands the stall margin, showcasing marked improvements over traditional designs. For perspective, conventional high-lift devices [8] are inherently passive, relying on the incoming airflow to generate a high-speed jet through available gaps. This approach serves to enhance aerodynamic forces and protract the onset of stall, often accompanied by an increased curvature. However, in juxtaposition, the CFJ technology offers an adaptable control over air volume, permitting operations under a broader and more intricate range of conditions.

Drawing inspiration from bionics [9], this technique emulates the high circulation achieved by the vibrating wings of birds and insects. These biological systems support their weight by creating a potent low-pressure suction at the leading edge, resulting in a net thrust for forward flight [10]. Such observations culminated in the development of the CFJ technique [11], wherein a zero-net-mass flux jet augments momentum to the external flow field without incurring mass loss. Furthermore, jet and free-stream interactions amplify lateral energy transfer. This innovative approach yields salient benefits: a marked lift augmentation, drag reduction, and an expanded stall margin. Both experiments and simulations have corroborated these merits. Preliminary wind tunnel investigations [12] attested that the outstanding aerodynamic performance of the CFJ-NACA-0025 airfoil was both feasible and reliable using high-pressure and low-pressure cylinders as the zero-net-mass flux gas sources. Subsequent studies probed the influence of the size [13] and positioning [14, 15] of injection and suction nozzles on aerodynamic coefficients. Parameters gauging the strength [16], exhaust momentum coefficient, and the reaction force equations for the nozzles were pivotal in refining lift and drag coefficients in numerical models [17]. Collectively, these investigations sculpted the foundational framework of the CFJ technology. With escalating industrial advancements, the quest for eco-friendly vehicles [18] has emerged as a pivotal directive, catalyzing refinements in CFJ applications. Notably, wind tunnel tests of the CFJ-NACA-6421 airfoil, utilizing miniature compressors as an alternative to traditional cylinders, showcased its capability to exceed theoretical boundaries of the potential flow theory [19]. Explorations into ducted fan and culvert profile integration [20] have hinted at heightened jet utilization efficiency. Further advancements, such as the Discrete Co-Flow Jet (DCFJ) technique [21], aim to intensify the jet-free stream mixing through a segmented nozzle area, ensuring optimal energy dispersion by the zero-net-mass flux. Despite the increased power demand for the internal apparatus, this technique significantly bolsters energy conversion rates. Empirical evidence from wind tunnel analyses on the DCFJ-OA312 airfoil suggests a potential 67.3% enhancement in maximum lift coefficient and a 12° delay in stall angle [22]. Additionally, there have been innovations like the pulsed co-flow jet technology [23], optimizing power usage, and the plasma co-flow jet [24], which investigates the feasibility of replacing traditional ducted fans with plasma brakes. From a computational perspective, methodologies such as RANS [25], DES [26], and IDDES [27] have been instrumental in dissecting the aerodynamic characteristics of the CFJ across varying angles of attack and Mach numbers. Investigations into wall separation, co-flow jet controls [28], and applications of CFJ across rotor blades [29], boosters [30], flaps [31], wind airfoils [32], dynamic stall phenomena [33], and integrated wing-body vehicles have further broadened the technology's horizon.

In the realm of wind tunnel testing for CFJ airfoils, the phenomenon of wall effects poses intricate challenges. Specifically, these effects can induce perturbations that constrict the jet proximal to the wall, thereby influencing the aerodynamic forces exerted on the entire airfoil. Such complications have downstream consequences, leading to potentially skewed pressure readings at the airfoil's mid-span. Furthermore, abrupt pressure variations at the CFJ airfoil's inlet and outlet necessitate elevated levels of experimental precision. To address these multifaceted challenges, this paper introduces an experimental methodology specifically tailored for the wind tunnel testing of two-dimensional

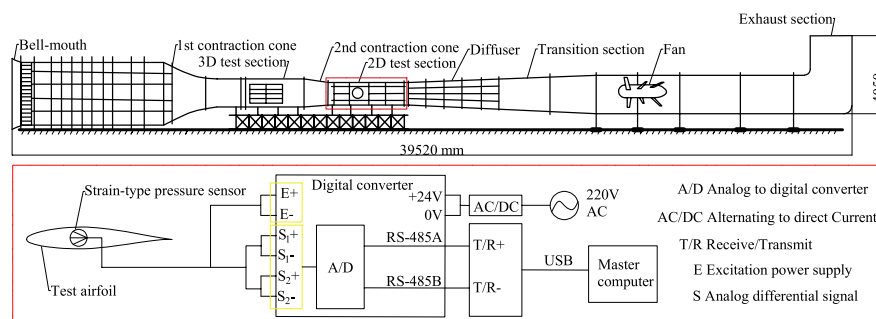


**Fig. 1** Schematic diagram of the overall structure and dimensions of the wind tunnel. The experimental position of the red frame airfoil in the wind tunnel and the specific signal transmission path

CFJ airfoils. The devised approach not only enables the direct acquisition of aerodynamic metrics pertinent to the CFJ airfoil but also mitigates the distortive impact of wall effects. Critically, the scheme has been designed to circumvent sudden pressure alterations at the injection and suction nozzles, thereby enhancing the fidelity of the experimental measurements. Comparative analysis of the experimental findings with numerical simulations serves to substantiate the reliability and robustness of the newly formulated experimental paradigm.

## 2 Wind tunnel experiment scheme

### 2.1 Wind tunnel equipment

In this research, the Low Turbulent Wind Tunnel (LTWT), an advanced low-speed, low-noise, and low-turbulence direct-current wind tunnel, is utilized for testing. A schematic of this facility can be found in Fig. 1.

The LTWT wind tunnel spans a length of 39.52 m and stands at a height of 4.05 m, incorporating a blend of ternary and binary experimental segments. Dimensions for the three-dimensional experimental compartment are  $1.05\text{ m} \times 1.2\text{ m}$ , while its two-dimensional counterpart measures  $0.4\text{ m} \times 1\text{ m}$ . The contraction section is bifurcated: the initial segment boasts a contraction ratio of 7.11, succeeded by a section with a ratio of 3.18. Collectively, the aggregate contraction ratio sums to 22.6. Experimental evaluation of the OCFJ airfoil was undertaken within the two-dimensional segment. Aerodynamic measurement of the airfoil was performed using a strain-type pressure sensor. A comprehensive elucidation of the measurement signal's transmission mode will be presented in subsequent sections detailing the experimental apparatus.

### 2.2 Experimental airfoil and scheme design

Figure 2 illustrates the design concept behind the CFJ airfoil. This design incorporates an air inlet positioned at the lowest pressure point on the leading edge and an air outlet at the trailing edge. In this context, the subscript 1 refers to injection, while the subscript 2 signifies suction. The air released from the injection is subsequently drawn back into the suction, leading to the establishment of a recirculating flow pattern. Such a mechanism generates a zero-net-mass flux jet, ensuring there is no loss in jet mass. The

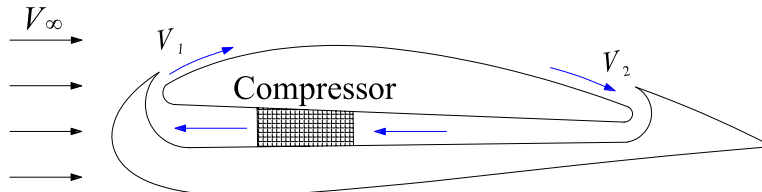


**Fig. 2** Flow pattern of zero-net-mass flux jet in the CFJ airfoil. The blue arrow line is the jet flow, and the black arrow line is the free stream

primary advantage is that this design solely dissipates energy into the surrounding flow field without a net loss of mass. Furthermore, the injection is strategically positioned at the maximum pressure point on the airfoil's leading edge. This arrangement augments the flow of the jet, facilitating smoother egress from the injection slot. Conversely, the elevated pressure on the trailing edge enhances the intake into the suction slot. Additionally, the low pressure at the leading edge of the nozzle creates an upward drag on the airfoil's upper surface, which exerts a longitudinal attraction on the jet. It intensifies the mixing of the free stream and the jet, increasing the energy transfer and achieving the goal of controlling the circulation to improve the aerodynamic performance of the airfoil.

For co-flow jet airfoils, the most critical parameter [16] is the jet momentum coefficient ( $C_\mu$ ) of the injection nozzle, which characterizes the strength of the jet and is expressed as:

$$C_\mu = \frac{\dot{m}V_1}{\frac{1}{2}\rho_\infty V_\infty^2 S}, \quad (1)$$

where  $\dot{m}$  is the mass flow rate,  $V_1$  is the velocity of the injection inject,  $\rho_\infty$  is the density of the free stream,  $V_\infty$  is the velocity of the free stream, and  $S$  is the reference area of the airfoil.

The power coefficient of the compressor characterizes the energy consumption of the compressor. This coefficient is determined by the power of the compressor, which is defined by the thermodynamic formula.

The power ( $P$ ) of the compressor is:

$$P = \frac{\dot{m}c_p T_2}{\eta} \left( \left( \frac{P_1}{P_2} \right)^{\frac{\gamma-1}{\gamma}} - 1 \right). \quad (2)$$

The power coefficient ( $P_c$ ) is:

$$P_c = \frac{P}{\frac{1}{2}\rho_\infty V_\infty^3 S}. \quad (3)$$

In the formula,  $c_p$  is the constant pressure-specific heat capacity constant,  $T_2$  is the total temperature at the suction, and  $\eta$  is the compressor efficiency (meaning the compressor energy conversion power, which is taken as 1 in this paper),  $P_1$  and  $P_2$  is the total pressure of the injection and the suction, respectively.  $\gamma$  is the specific heat ratio (value 1.4).

The corrected aerodynamic efficiency ( $k$ ) is:

$$k = \frac{C_l}{C_d + P_c}. \quad (4)$$

In the formula,  $C_l$  represents the lift coefficient and  $C_d$  represents the drag coefficient.

The introduction of the corrected aerodynamic efficiency comprehensively considers the relationship between the energy consumption of the compressor and the additional aerodynamic force it provides.

Based on the flow mechanism of the co-flow jet and the wind tunnel's dimensions, the CFJ6421 has a chord length and a span length of 0.4 m. The injection and suction slot heights are 0.65% (2.6 mm) and 1.42% (5.68 mm) of the chord length, respectively. The injection and suction slots are positioned at 5% and 80% of the chord length, respectively.

As per our previous study [34], the airfoil used in the experiment was the optimized co-flow jet 6421 (OCFJ6421) airfoil. This airfoil is an improvement over the CFJ6421 airfoil achieved by coupling and optimizing the CFJ technology with the parametric shape. Table 1 shows the design variables  $c_i$  used in optimizing the OCFJ6421 airfoil. This multi-objective global optimization used the Hicks-Henne shape function [35] for parametric modeling. Fourteen design variables were set on the upper and lower wings of the airfoil, and the objective functions optimized were the aerodynamic performance, lift increase efficiency ratio, and drag reduction efficiency ratio [36]. Under specific experimental conditions ( $M_\infty = 0.0147$ ,  $Re = 1.33 \times 10^5$ ,  $C_\mu = 0.079$ ,  $\alpha = 2^\circ$ ), the optimized airfoil improved the lift coefficient by 11.75% and reduced the drag coefficient by 17.22%.

To obtain more accurate measurements of the aerodynamic parameters of the OCFJ6421 airfoil in a two-dimensional wind tunnel and to minimize the effects of the wall effect, an innovative design was implemented, as depicted in Fig. 3.

In designing the experimental setup, initial considerations are given to the dimensions of the wind tunnel and the maximum permissible obstruction ratio. These factors guide the selection of an appropriate model size and the specifications for the ducted fans. The experimental model is subsequently partitioned into three segments: a central experimental section flanked by fixed sections at either end. A 1 mm gap is intentionally placed between the experimental and fixed sections to mitigate interference originating from the latter. The central experimental section is explicitly engineered for aerodynamic measurements, while the fixed sections are incorporated to attenuate experimental anomalies attributable to wall effects within the wind tunnel. To ensure homogeneous distribution of zero-net-mass flux jet intensity along the airfoil's span, two ducted fans are mounted within the experimental section, with a fan installed in each of the fixed sections. During the assembly phase, the airfoil in the experimental section is affixed to a supporting rod via a strain-type pressure sensor. This setup ensures that the airfoil remains in contact solely with the pressure sensor, thereby minimizing extraneous

**Table 1** Design variables  $c_i (\times 10^{-2})$  [34] of the OFJ6421 airfoil in optimization. From 1 to 7 is from the leading edge to the trailing edge

Baseline	$c_1$	$c_2$	$c_3$	$c_4$	$c_5$	$c_6$	$c_7$
Upper	0.0583154	0.170103	0.6839475	1.3492515	0.7583871	0.265861	-0.0171801
Lower	-0.7997711	-0.4648966	0.4963607	0.4949874	0.0188144	0.262501	-0.8695659

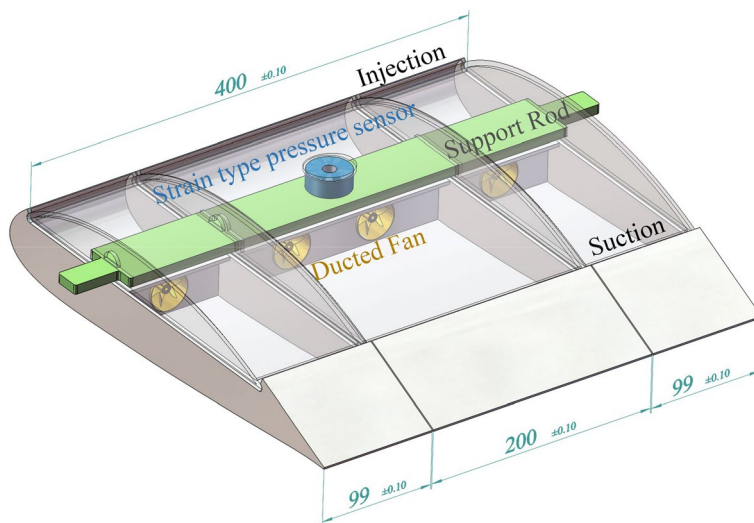


**Fig. 3** Perspective view of the 3D experimental OCFJ airfoil model. (multimedia view: go to see the [Video online](#))

interactions. The fixed sections are securely fastened to both the supporting rod and a rotating window. This rotating window feature enables adjustments in the angles of attack of the airfoil during experimentation. To measure the static pressure at the injection nozzles, holes are drilled into the surface of the airfoil, positioned directly beneath the nozzles. Since the experiment was conducted under low-speed flow conditions and the external atmospheric pressure remained constant, the total pressure can be represented as the sum of static and dynamic pressure according to Bernoulli's equation. Subsequently, the velocity of the jet at the injection nozzle can be ascertained by measuring the static pressure on the wind tunnel wall and the wind speed. The physical model is shown in Fig. 4.

The experimental airfoil is manufactured using 3D printing technology with acrylonitrile-butadiene-styrene as the printing material. The airfoil's surface is polished and finished, and its overall size measures 400 mm × 400 mm. The required surface roughness for the airfoil is  $R_a$  0.8. The support rod is made of aluminum alloy material, which can

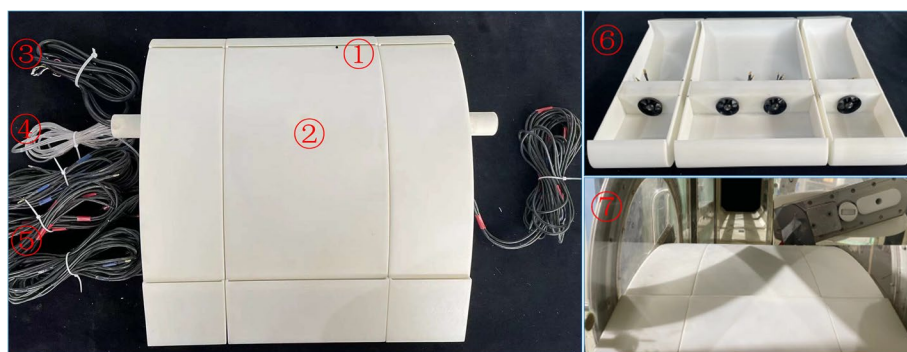


**Fig. 4** ① Static pressure tap; ② Location of the strain-type pressure sensor; ③ Connection line of the strong type pressure sensor; ④ Connection line for static pressure measurement at injection; ⑤ Power supply line of induced fan. ⑥ Lower part of airfoil with ducted fans; ⑦ Connection mode of airfoil and wind tunnel wall

support the weight of the entire airfoil without affecting the accuracy and precision of measurement due to bending deformation. The airfoil consists of two parts: the upper cavity, which includes a static pressure measuring copper tube with the injection nozzle and a strain-type pressure sensor, and the lower cavity, which contains ducted fans. The static pressure measurement hole is located directly before the ducted fan to ensure uniformity and minimal disturbance. The sensor is positioned at 30% of the chord length from the leading edge in the middle of the airfoil experimental section to minimize its distance from the center of pressure. The fixed section is half the size of the experimental section and is directly fixed to the support rod and rotating window. One tunnel fan is arranged in the fixed section, and two tunnel fans are arranged in the experimental section to ensure uniform jet strength at equal power. The support rod is equipped with a fixing ring to fit the wind tunnel rotating windows. When installing the internal components, it is essential to pay special attention to the arrangement of the strain-type pressure sensor and the pressure-measuring copper tube to ensure accurate measurements, as shown in Fig. 5. The airfoil experimental section should only be connected to the support rod through the strain-type pressure sensor, and one side of the sensor should be connected to the support rod using a countersunk hexagonal screw of M10, while the other side is glued to the upper surface of the wing using modified silane polyether.

In the installation of the pressure-sensing copper tube, a generous amount of modified acrylate adhesive is applied to fix the tube's position securely. This ensures that the measurement port of the pressure-sensing copper tube remains perpendicular to the airfoil surface, thereby enhancing the sensitivity and accuracy of pressure measurements.

Beyond the basic airfoil model, the comprehensive experimental apparatus incorporates two distinct electrical systems. The first system delivers regulated direct current (DC) power to the ducted fans and governs their output performance. The second system similarly provides regulated DC power, but directs it to the sensors and is responsible for collecting digital signals during experimentation, as illustrated in Fig. 6.

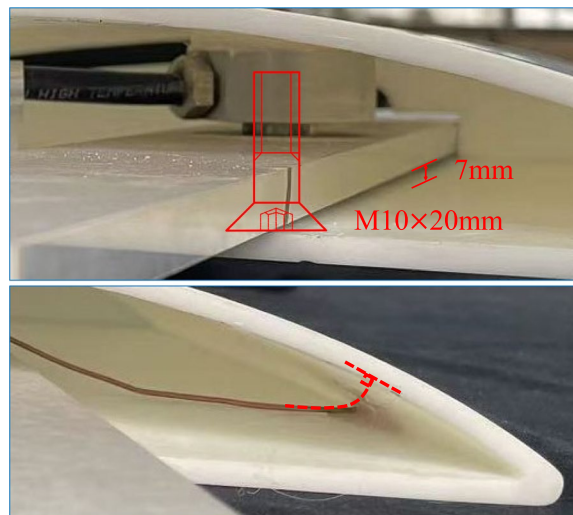


**Fig. 5** The connection mode of the support rod, strain-type pressure sensor, and experimental section airfoil (up). The installation mode of the copper pipe for injection nozzle static pressure hole measurement (down)

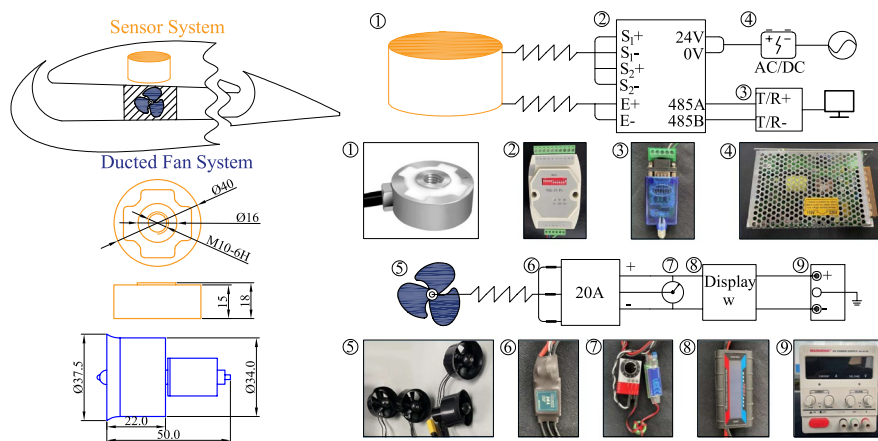


**Fig. 6** Sensor system and ducted fan system. From left to right is: ① strain-type pressure sensor, ② 4-way weighing acquisition module, ③ RS-485 protocol information conversion and transmission module (Input/Output interface), ④ alternating current (AC) to direct current (DC) power converter, ⑤ 30 mm ducted fans, ⑥ electronic speed control, ⑦ tester of electronic speed control and ultra-battery-elimination-circuit module, ⑧ digital display adjustable direct-current-regulated power supply, ⑨ high-precision watt meter and power analyzer

In the ducted fan system, 14.8V regulated power is supplied to the system by MAISHENG<sup>TM</sup> DC power supply MS-1030D. Four 35 mm diameter QF1611-5000KV ducted fans are used, which are driven by 20A electronic speed control and combined with a regulator to control the speed. The high-precision watt meter and power analyzer detect whether the fan power and speed reach the experimental target under each experimental condition and adjust the power to test each specific experimental state.

The sensor system is customized with a strain-type pressure sensor of  $\phi 40 \times 18$  mm in a two-axis force direction. The 220V AC power is converted to 24V DC power supplied to the four weighing acquisition modules by MW<sup>TM</sup> MS-150-24 AC/DC power converter. The four-way weighing acquisition module provides the excitation power for the strain-type pressure sensor, receives the analog differential signal generated by the sensor, converts the signal into a digital signal by the built-in circuit, and transmits the signal via the RS-485 protocol, and then transfers it to the upper computer after conversion by the Input/Output interface to record the experimental parameters.

### 3 Numerical calculation method

#### 3.1 CFD methods

In the right-angle coordinate system  $\Omega \in \mathbb{R}^3$ , the Reynolds-Averaged Navier-Stokes (RANS) equations can be described as:

$$\frac{\partial}{\partial t} \iiint_{\Omega} \mathbf{Q} d\Omega + \oint_{\partial\Omega} \mathbf{F}_c \cdot n d\mathbf{S} = \oint_{\partial\Omega} \mathbf{F}_v \cdot n d\mathbf{S}, \quad (5)$$

where  $\partial\Omega$  is the boundary of the control body  $\Omega$ ,  $n$  is the outer normal vector of the boundary,  $\mathbf{Q}$  is the conservation variable,  $\mathbf{F}_c$  is the inviscid flux,  $\mathbf{F}_v$  is the viscous flux, and  $d\mathbf{S}$  is the surface area of the control volume of unit norm  $n$ .

The effective viscosity of a fluid is a combination of turbulent viscosity and molecular viscosity. We have selected the Shear Stress Transfer (SST)  $k - \omega$  turbulence model [37] to model the turbulent viscosity. On the other hand, molecular viscosity is obtained by interpolating the Sutherland formula based on the temperature and pressure during the experiment. To determine the boundary flow information, we use Riemann invariants combined with the ideal gas equation to calculate the pressure-far-field, which is then used as a boundary condition for the flow field. The mass-flow-inlet boundary condition is assumed at the injection to ensure that the jet of the CFJ is zero-net-mass, and the pressure-outlet boundary condition is assumed at the suction. During the calculation process, it is necessary to perform several iterations to ensure that the pressure at the suction matches the mass flow of the flow field at the injection. The specific value of the mass flow boundary at the injection is determined according to the measured value of the wind tunnel experiment, so the flow conditions are  $(M_\infty, Re) = (0.0147, 1.33 \times 10^5)$ . The pressure-based coupled scheme in the software ANSYS Fluent simulates the low Mach number flow.

### 3.2 Grid generation

Two sets of numerical grids are generated for the paper. Grid 1 is shown in Fig. 7 and is used to compute the flow around the co-flow jet airfoil in a free environment. Grid 2 is shown in Fig. 8 and is used to simulate the actual experimental process.

The flow field configuration for Grid 1 employs an H-shaped grid, designed to maintain grid orthogonality. Boundary conditions surrounding this flow field utilize a far-field pressure boundary positioned 100 times the model's chord length away. This is to minimize the influence of boundary flows on the airfoil during computations. Both lateral boundary conditions are designated as symmetric surfaces, ensuring that three-dimensional effects do not distort results. In the vicinity of the airfoil, the grid utilizes an O-block mesh topology, an effective solution for addressing grid distortions occurring at vertices of circular arcs or other intricate geometric block configurations. This approach also facilitates the generation of an optimal boundary layer encryption near

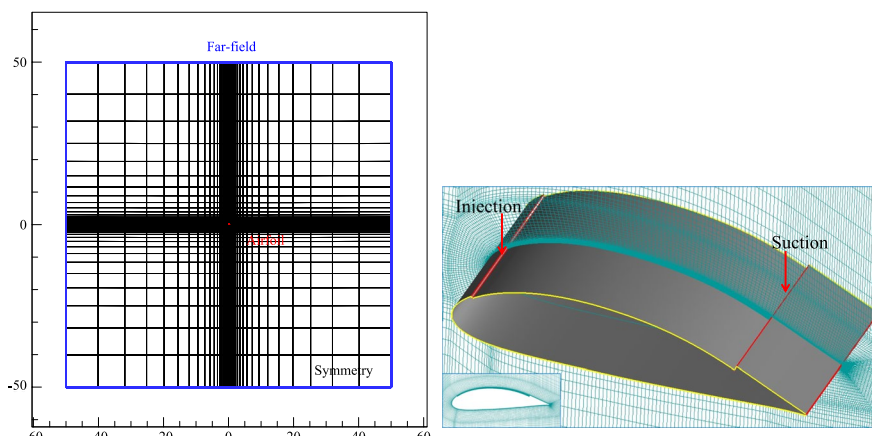


**Fig. 7** Grid 1. Which is used to simulate the flow around the airfoil in a free environment. The yellow line represents the symmetry plane that contacts the airfoil, while the red line represents the wall surface that contacts the airfoil. Model dimensions: (chord length  $\times$  span) = (400 mm  $\times$  200 mm)

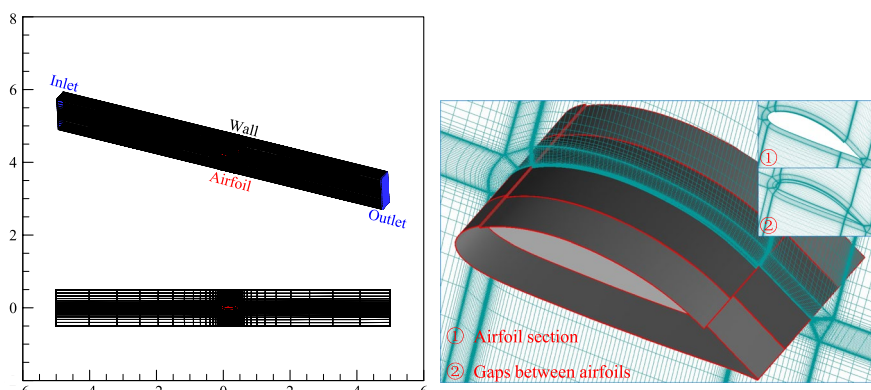


**Fig. 8** Grid 2. Which is used to simulate the flow around the airfoil in a wind tunnel. Model dimensions: (chord length  $\times$  span) = (400 mm  $\times$  400 mm) and the gap is 1 mm

the wall surface. The grid density is intentionally heightened around the injection and suction nozzles, targeting precise capture of the mixing dynamics between the jet and the ambient flow. The dimensionless parameter  $y+ \simeq 1$  guarantees the initial grid spacing between the fluid and the wall aligns with computational prerequisites. Grid 1 is comprised of 1.31 million cells and is partitioned into 32 blocks to accommodate parallel computations.

For Grid 2, the foundational grid topology mirrors that of Grid 1. However, to refine the grid quality, the gap separating the airfoil test and fixed sections is structured with dual O-blocks. Unlike Grid 1, Grid 2 is designed to mimic real wind tunnel conditions, necessitating distinctive boundary conditions. The flow field inlet employs a velocity inlet boundary, while a pressure outlet boundary is designated for the outlet. All remaining boundaries are treated as non-slip walls. The flow field's dimensions reflect the actual dimensions of the wind tunnel. Grid 2 consists of 2.87 million cells and is also divided into 32 blocks to facilitate parallel computations.

### 3.3 Grid convergence verification

Given the identical grid density and generation method of Grid 2 to that of Grid 1, and the congruent subsequent computational conditions, the necessity for grid convergence verification is limited solely to Grid 1 in this research. Grid 1 is structured as an H-type grid. Specifically, it has 40 nodes arranged spanwise along the wing, 350 nodes oriented circumferentially, 37 nodes designated for the wing's boundary layer, 35 nodes circumferentially outside the boundary layer, and 33 nodes allocated for both the injection and suction nozzles. The grid nodes throughout the entire model will be increased and decreased by 20% to verify the convergence of the grid. Since the boundary layer grid distribution was determined based on the  $y+$  criteria, there will be no changes to the boundary layer grid layout. Figure 9 shows a 20% reduction in the number of grid nodes in all directions.

The lift and drag coefficients were calculated under three different conditions (Con. 1; Con. 2; Con. 3) = ( $V_1 = 12.02$  m/s,  $\alpha = 0^\circ$ ;  $V_1 = 12.84$  m/s,  $\alpha = 4^\circ$ ;  $V_1 = 14.15$  m/s,  $\alpha = 8^\circ$ ) for three sets of grids at the computational condition of ( $M_\infty, Re$ ) = ( $0.0147, 1.33 \times 10^5$ ). The results are presented in Table 2.

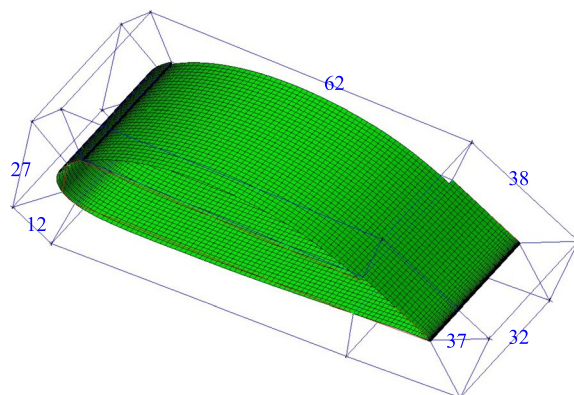


**Fig. 9** Airfoil grid with a 20% reduction in grid quantity

**Table 2** Verification of aerodynamic parameters for convergence of aerodynamic grids

Conditions	$C_l$			$C_d$		
	Con. 1	Con. 2	Con. 3	Con. 1	Con. 2	Con. 3
Grids						
Grid 1 (-20%)	1.0287	1.5215	2.0317	-0.00263	-0.00243	-0.00219
Grid 1	1.0291	1.5218	2.0319	-0.00258	-0.00239	-0.00224
Grid 1 (+20%)	1.0293	1.5221	2.0320	-0.00257	-0.00237	-0.00224

As can be observed from Table 2, the deviation in the computed aerodynamic parameters is less than 1% under different grid quantities. Therefore, the number of grids in Grid 1 is appropriate, exhibiting good grid convergence. The quantity and size of this grid meet computational requirements, and the slight influence on numerical computation parameters can be disregarded.

#### 4 Results and discussion

If the wind speed in the wind tunnel is too fast, a large amount of power is required for the ducted fan. At the same time, the material of the experimental model is hard resin, which can deform aero elastically when subjected to excessive lift forces, thus affecting the accuracy of the experiment. Therefore, a wind speed of 5 m/s was selected as the free stream for the experiment. The experimental wind tunnel was situated in an environment with an atmospheric pressure ( $P_0$ ) of 97,820 Pa and a temperature ( $T_0$ ) of 287.05 K. A total of 18 states of the CFJ airfoil were measured throughout the experiment. The aerodynamic states of the airfoil at the angles of attack of 0° to 10° with each ducted fan operating at different powers ( $P = 10$  W, 20 W, and 30 W). The high-precision watt meter and power analyzer accurately measure and display the whole power consumption of various components in a ducted fan system, so we can use the watt meter data as the basis to control the rotation speed of the ducted fan.

The instrument measures the static pressure of the wind tunnel under experimental conditions, and it is known that the static pressure of the wind tunnel at this time is

97,792 Pa. The static pressure value measured at the blowing port can be converted to obtain the velocity of the injection nozzle, as shown in Table 3.

In scenarios where the power of the internal ducted fans within the OCFJ airfoil is elevated, several consequences follow. Firstly, an increase in fan speed is observed, leading to augmented thrust generation. Secondly, a concomitant decline in static pressure is recorded at the injection nozzle, which culminates in a heightened jet speed and elevated mass flow rate. As the angle of attack ascends, the static pressure at the injection nozzle further diminishes while the jet speed escalates, even under consistent motor power. This phenomenon is attributed to the amplified negative pressure zone engendered by the airfoil's leading edge at elevated angles of attack; the greater the angle, the more pronounced the negative pressure, thereby driving an increased jet at a constant power level. Table 3 elucidates that the growth in jet velocity is more pronounced when the ducted fan power is escalated from 10 W to 20 W, as opposed to the increment between 20 W and 30 W. This implies that the relationship between jet speed and fan power is not linear. A disproportionate amount of energy is expended in driving the ducted fan to achieve incremental increases in jet velocity.

The aerodynamic performance parameters of the OCFJ airfoil obtained from the wind tunnel test and numerical simulation are shown in Figs. 10 and 11. Simulation 1 is the calculation result of Grid 1, the flow around the CFJ airfoil in a free environment, and simulation 2 is the calculation result of Grid 2, which is the flow around the CFJ airfoil under experimental conditions.

The wind tunnel test and simulation data show an excellent linear change rule, and the error between them is relatively small. The coincidence degree of lift and drag coefficients in numerical value and change rule is relatively high. Some of the differences come from the numerical accuracy of the RANS simulation and the truncation error caused by the range of the strain-type pressure sensor, especially the drag coefficient. The change in its value comes from the percentile after the decimal point, which is more affected by the accuracy of the measuring instrument. Other differences come from the comprehensive error caused by objective factors such as experimental conditions and the tunnel wall effect. However, in general, the wind tunnel test results meet the requirements, and the experimental model is feasible according to the design scheme, which achieves the purpose of the wind tunnel test. To further reduce the discrepancies

**Table 3** Depending on the unique effect of the co-flow jet technology on the aerodynamic characteristics of the airfoil, the design variables at different locations on the upper surface are taken at different values from experience

P (W)	Static pressure (Pa)			velocity (m/s)		
	10	20	30	10	20	30
$\alpha$ (°)						
0	97,761	97,738	97,721	8.79	10.77	12.02
2	97,756	97,732	97,717	9.25	11.23	12.30
4	97,751	97,727	97,709	9.78	11.59	12.84
6	97,747	97,721	97,699	9.95	12.02	13.48
8	97,740	97,710	97,693	10.61	12.77	14.15
10	97,732	97,703	97,685	11.23	13.22	14.32

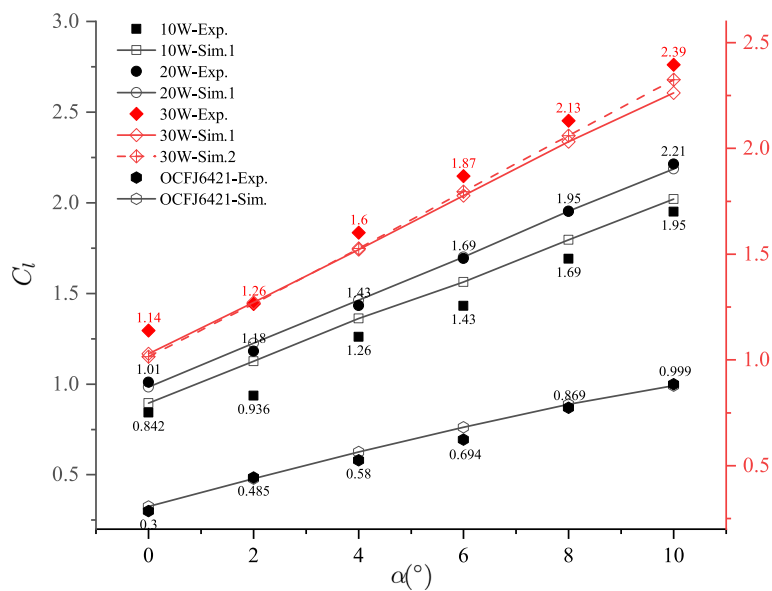


**Fig. 10** Variation of the lift coefficient of the OCFJ airfoil with angles of attack in wind tunnel experiments and numerical simulations. Exp. stands for experiment results and Sim. is simulation results. Experimental and simulation conditions:  $(M_\infty, Re, T_0, P_0) = (0.0147, 1.33 \times 10^5, 287.05 \text{ K}, 97,820 \text{ Pa})$

between experiments and simulations, starting from the experimental perspective, one can use more accurate measuring equipment to minimize truncation errors. Moreover, increasing the resolution of the measurement plane is essential to capture key features of the flow field. Reducing the surface roughness of both the wind tunnel and the model is beneficial, as well as ensuring the stability of environmental conditions such as wind speed, temperature, and humidity. From a simulation viewpoint, it's crucial to choose an appropriate turbulence model and high-precision numerical methods, ensuring the right time step and boundary conditions. By continuously iterating through multiple experiments and simulations, the model can be refined and improved.

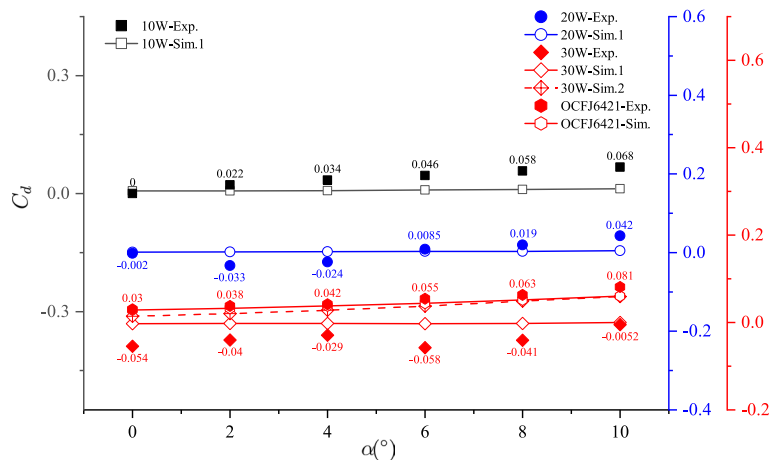


**Fig. 11** Variation of the drag coefficient of the OCFJ airfoil with angles of attack in wind tunnel experiments and numerical simulations

Secondly, through numerical simulations to evaluate the incorporation of co-flow jet technology in the OCFJ6421 airfoil, it becomes unequivocally clear that this technology yields substantial improvements in aerodynamic performance. The computational results show marked enhancements in both lift and drag coefficients across a range of angles of attack. These improvements are observed across various power settings for the ducted fan system. Specifically, when operating at a power consumption level of 10 W, the airfoil sees an average lift coefficient increase of 123.2% and an average drag coefficient reduction of 75.0%. When the power level is elevated to 20 W, these metrics improve further, yielding an average lift coefficient increase of 142.6% and a drag coefficient reduction of 97.6%. At a power setting of 30 W, the simulations suggest an average lift coefficient increase of 152.6% and an average drag coefficient reduction of 114.5%. These empirical results offer robust validation for the efficacy of co-flow jet technology in significantly optimizing the aerodynamic performance of airfoils.

The corrected aerodynamic efficiency metric incorporates the energy consumption of the compressor, serving as a critical marker for assessing energy conservation. Figure 12 illustrates the trend of the revised aerodynamic efficiency of the CFJ airfoil with respect to variations in the angle of attack. Upon activation of the jet, the airfoil realizes an enhancement in aerodynamic performance that outweighs the energy expenditure of the compressor. Considering the blunt leading edge characteristic of the OCFJ6421 airfoil, the absence of jet utilization leads to a transition in the airfoil's aerodynamic efficiency from an increasing to a decreasing trend beyond a 6° angle of attack. Conversely, employing the jet fosters a sustained increase in aerodynamic efficiency within a 0° ~ 10° angle of attack interval. Moreover, as delineated by Figs. 10, 11, and 12, despite the superior lift and drag reduction capabilities offered by a higher-powered jet under uniform angle of attack conditions, a continuous escalation

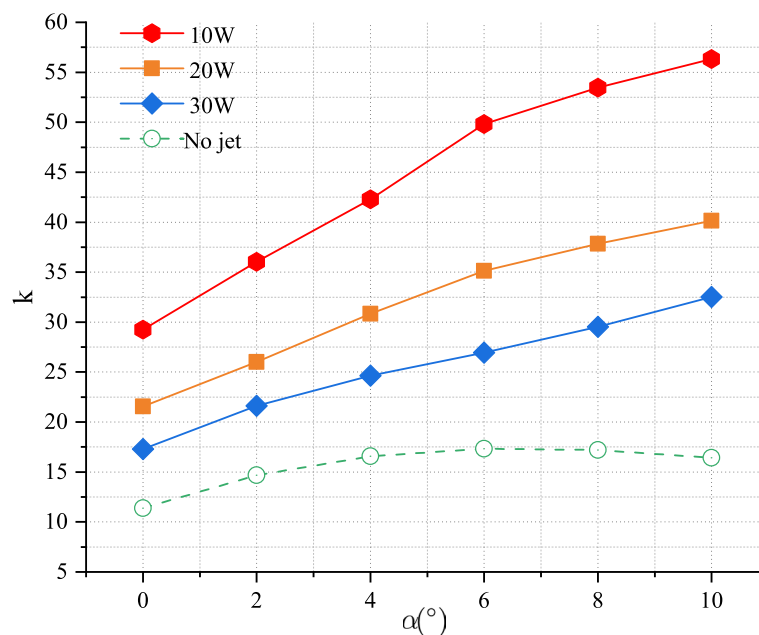


**Fig. 12** The corrected aerodynamic efficiency varies with the angle of attack in Simulation 1

in system power precipitates a gradual decline in the airfoil's aerodynamic efficiency. Consequently, an upward trend in compressor power heralds a diminishing return in the aerodynamic efficiency of the CFJ airfoil.

Figure 13 presents the pressure distribution cross-section for the OCFJ airfoil flow field. Observing the baseline airfoil, it becomes evident that as the angle of attack consistently escalates, there is a forward shift in the pressure center, with an expanding low-pressure zone on the upper surface of the airfoil leading edge, and an augmenting negative pressure peak. The CFJ airfoil behavior aligns with this principle. Notably, the injection nozzle of the co-flow jet airfoil is located at the leading edge, and the high-speed co-flow jet increases the circulation around the airfoil while providing a higher negative pressure. According to the Kutta-Joukowsky condition, the variation of circulation is illustrated in Table 4. With an increase in jet strength, the negative pressure on the airfoil's upper surface intensifies, accompanied by an earlier forward shift of the negative pressure region. The airfoil's lower surface, in tandem with the increasing jet strength, experiences a greater positive pressure. Concurrently, due to the pronounced pressure differential between the airfoil's upper and lower surfaces, an extensive low-pressure zone is concentrated at the airfoil's leading

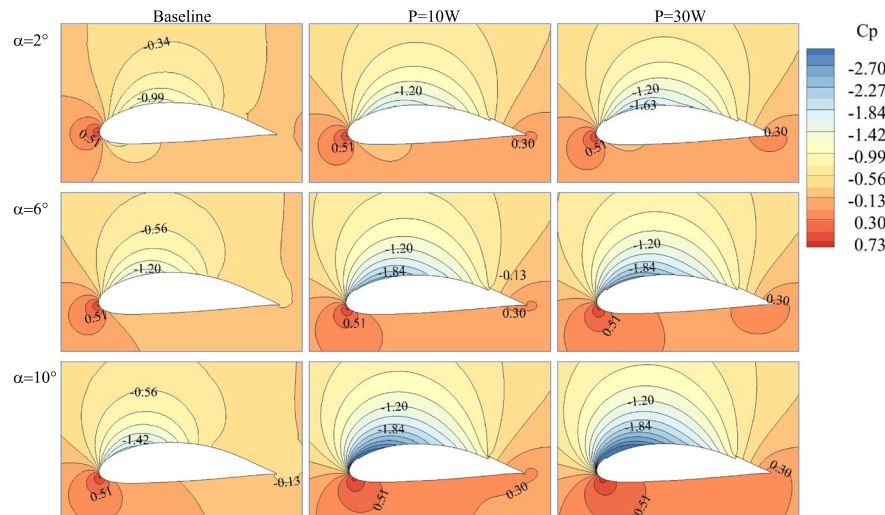


**Fig. 13** Pressure distribution of the flow field under different working conditions of the OCFJ6421 airfoil

**Table 4** The variation in circulation around the airfoil of Simulation 1. (Unit:  $\text{m}^2/\text{s}$ )

P (W)	10	20	30
$\alpha$ ( $^\circ$ )			
0	0.1790	0.1966	0.2058
2	0.2252	0.2450	0.2544
4	0.2723	0.2925	0.3044
6	0.3127	0.3401	0.3553
8	0.3592	0.3907	0.4064
10	0.4039	0.4374	0.4524

edge. This results in the formation of a positive pressure zone at the trailing edge, which becomes increasingly distinct with stronger jet intensities.

We analyze the streamline of the OCFJ6421 airfoil with no co-flow jet and with co-flow jets of different strengths for a  $10^\circ$  angle of attack in Fig. 14. The flow line distribution shows that when the OCFJ base airfoil is at the  $10^\circ$  angle of attack, flow separation already occurs at the middle and trailing edges of the airfoil, and a slower vortex is formed to attach to the airfoil's upper surface, at which time the airfoil exhibits a slight static stall tendency. When we disturb the flow field with a zero-net-mass flux co-flow jet, the vortex gradually weakens and disappears as the jet strength increases. Therefore, the co-flow jet technology can improve the stall margin of the airfoil, and the ability to suppress the stall increases with the jet intensity.

Referring to the experimental data calculated by numerical simulations, Fig. 15 shows the pressure distribution on the surface of the airfoil of simulation 2 at angles of attack from  $0^\circ$  to  $10^\circ$  at the power of 30 W. The two ends of the airfoil are fixed to the wind tunnel wall as the fixed section of the experimental model, and the middle section is the experimental section connected to the sensor. Since both sides of the fixed section are tunnel walls, there is a non-slip phenomenon on the wall's surface, generating a gradient of pressure and making the airflow near the near-wall surface unevenly distributed. The different flow velocities near the wall create an inward pressure due to the pressure difference at the surface. As a result, the flow field is disturbed, and the closer to the wall, the greater the effect. For these reasons, we have designed a wind tunnel model to reduce this effect, which aerodynamic measurements have verified well.

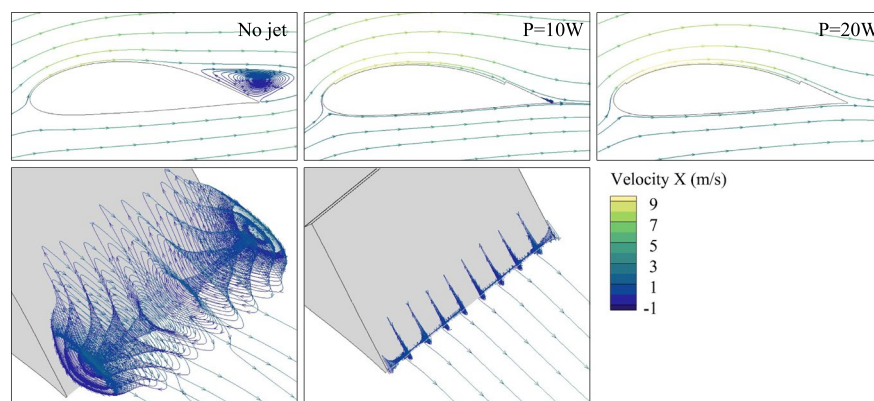


**Fig. 14** Pressure section and streamline (colored by velocity  $X$ ) distribution of the OCFJ6421 airfoil ( $\alpha = 10^\circ$ ) in Simulation 1

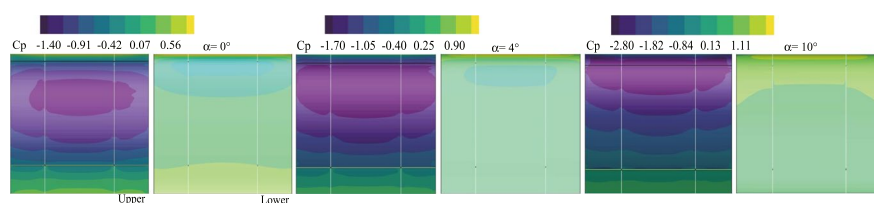


**Fig. 15** The pressure distribution on the airfoil's upper and lower surfaces in Simulation 2. Experimental and simulation conditions:  $(M_\infty, Re, T_0, P_0) = (0.0147, 1.33 \times 10^5, 287.05 \text{ K}, 97,820 \text{ Pa})$

In Fig. 15, the pressure distribution on the surface of the experimental section in the middle of the airfoil is more uniform when the gas flows over the surface. In the above view, the upper surface forms an elliptical or semi-elliptical negative pressure area similar to a court. While the middle experimental section is located in the middle parallel square area, and the fixed sections on both sides are affected by the wall effect, with the negative pressure decreasing and the flow velocity decreasing closer to the wall, as shown in Fig. 16. The same situation exists on the lower surface of the blade, but the flow changes on the lower surface are not as drastic as on the upper surface, and the pressure distribution in the experimental section is more uniform, while the fixed sections on both sides are still affected by the more severe wall effect.

Velocity cross-sections were taken along the airfoil span at intervals of 0.05 m, and velocities below 6.9 m/s were removed from the distribution in Fig. 16. Observing the velocity distribution along the airfoil's span reveals a trapezoidal shape influenced by the high-speed jet and the curvature of the airfoil. The velocity decreases outward from the surface of the airfoil. Moreover, due to the decreasing flow velocity above the airfoil, the effect of the wall boundary produces a more significant weight in the velocity change, resulting in a trapezoidal velocity distribution along the span. The influence is more pronounced near the wall on both sides of the chord section, while the measurement in the center is more evenly distributed. The four velocity sections exhibit similar characteristics in chord-wise velocity. This phenomenon is also visually evident in the flow 6.7 cm above the airfoil, as illustrated in Fig. 17.

Overall, the streamline distribution on the airfoil's upper surface appears relatively uniform. As the airflow passes over the experimental section of the airfoil, from the

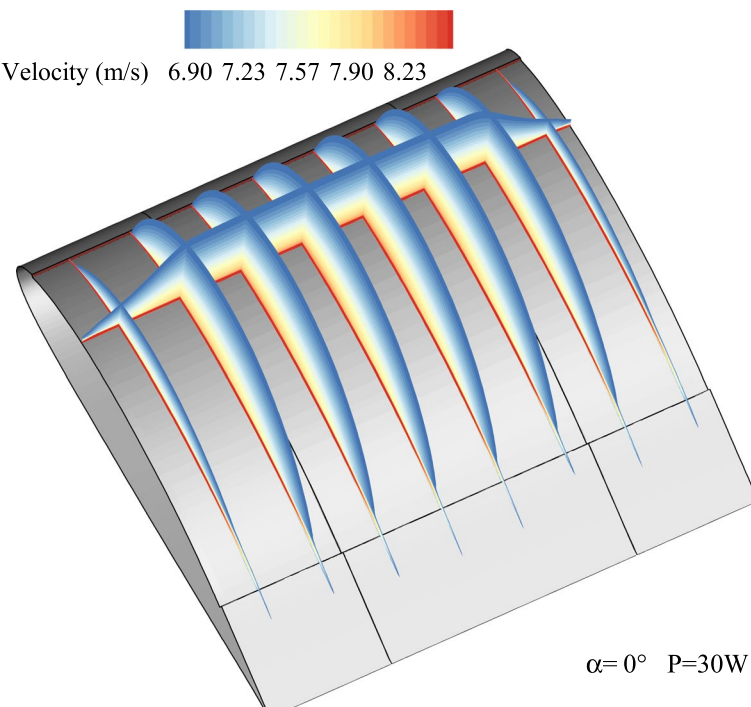


**Fig. 16** Velocity section of the OCFJ airfoil upper surface in Simulation 2

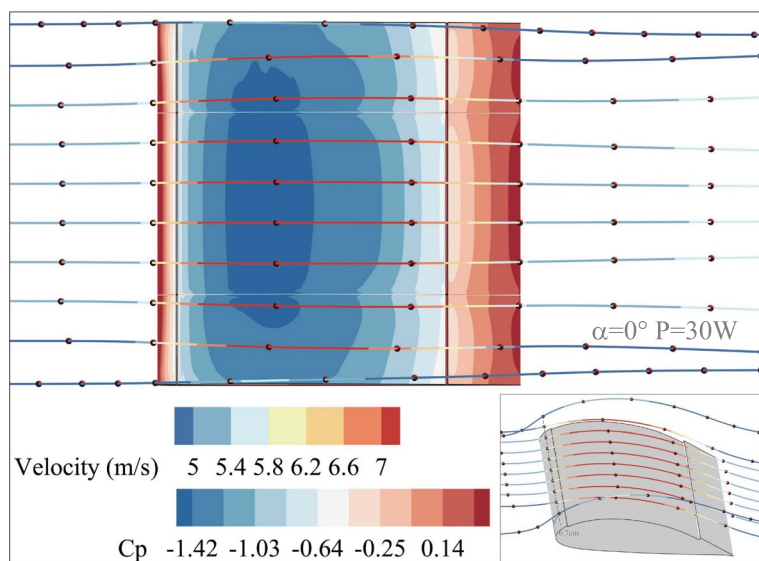


**Fig. 17** Streamline flow of the flow field at 6.7 cm (based on the leading edge) above the OCFJ airfoil.  
(multimedia view: go to see the [Video online](#))

leading edge to the trailing edge, the flow shows good consistency in acceleration and deceleration. The wall effect does not disturb the flow velocity above this section, reflecting good binary characteristics. However, the flow above the fixed section is influenced by the presence of the wall, resulting in lower velocities compared to the experimental section when viewed laterally. Additionally, the velocity gradually decreases near the wall. When viewed longitudinally, the flow velocity near the wall of the airfoil is slow, and the airflow passes from the lower horizontal plane of the leading edge 6.7 cm horizontal line to the higher horizontal plane and is compressed inward at the middle to the rear section of the airfoil, resulting in an inward deviation. Therefore, in the experimental model design, the aerodynamic forces of the airfoil near the wall are not measured, and the fixed section of the airfoil firmly attached to the wall is used to weaken the wall effect on both sides of the wall.

In the architectural layout of the experimental model, a 1 mm gap was engineered between the experimental and fixed sections. This was implemented to insulate the experimental section from any wall-effect interferences originating from the fixed section, which could potentially compromise the integrity of aerodynamic force measurements. While diminutive, this gap inevitably introduces some level of interference. Figure 18 illustrates the distribution of velocity vectors within this interstitial space. These vectors reveal that the airspeed over the airfoil's upper surface slightly outpaces that over the lower surface. This discrepancy gives rise to a translocation of airflow from areas of relatively higher pressure to those of lower pressure, subsequently generating a weak suction force and eliciting subtle three-dimensional effects. Although a minor upward flow tendency is observed, its influence attenuates as it transverses the gap and imposes negligible impact on the overarching flow dynamics across the upper surface. For an in-depth analysis of the surface flow in closest proximity to this gap, readers are directed to Fig. 19.

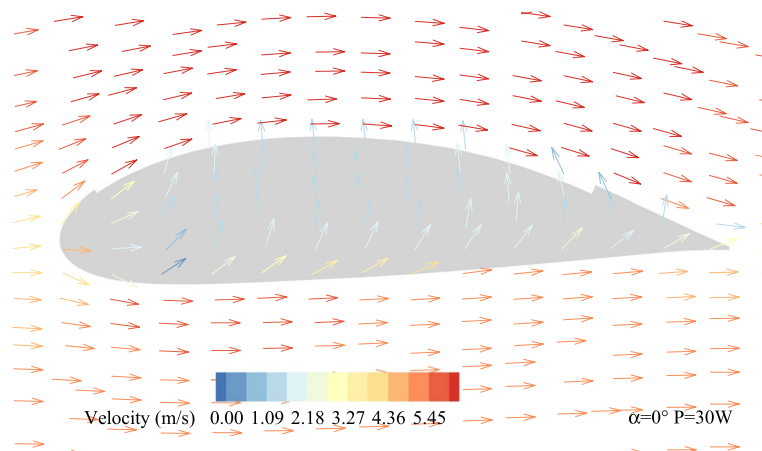


**Fig. 18** Velocity vector distribution of the 1 mm gap between the experimental section and the fixed section

The minor airflow from the gap to the airfoil's upper surface creates slight disturbances near the gap. The jet emitted from the edges of the co-flow jet airfoil's injection nozzle is affected by this airflow. As this airflow navigates through the mid and rear sections of the airfoil, there is an observable decline in jet velocity, accompanied by a slight upward deflection toward the airfoil's central region. Nevertheless, this phenomenon is localized and predominantly impacts the flow near the edges of the experimental airfoil. In the broader aerodynamic context, the ramifications of these disturbances are marginal. For heightened precision, future experiments could undertake a granular aerodynamic assessment aimed at further diminishing this effect. Potential strategies might encompass narrowing the relative width of the gap to attenuate flow disruptions, all while ensuring that the fixed and experimental sections remain aerodynamically independent.

The influence of the wall effect on wind tunnel experiments cannot be eliminated, which can increase measurement errors and distortion of the flow field. Its effect can

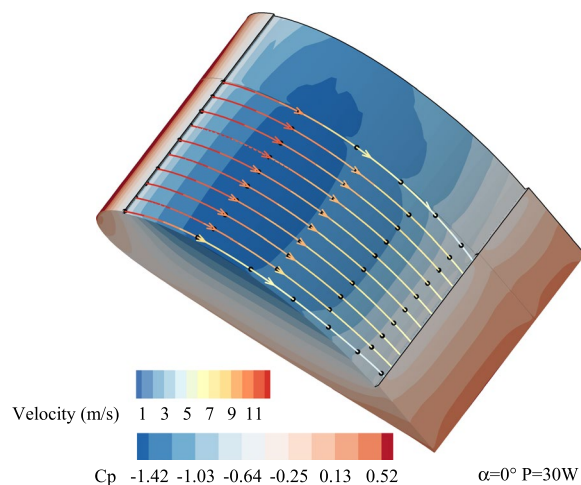


**Fig. 19** Airfoil surface pressure and jet streamline distribution in the experimental section

only be minimized by various technical means to obtain reliable experimental results. In the verification process of the CFJ airfoil aerodynamic force wind tunnel experiment, the three-section airfoil distribution method designed by us and the design of the fixed sensor and support rod used to support the experimental model can effectively reduce the interference of the left and right walls on the measurement of the CFJ airfoil aerodynamic force in the experimental section. The atmospheric environment data and the jet velocity of the injection nozzle were obtained practically by experiment, and the above parameters were used to perform numerical simulations of the CFJ airfoil under a free environment and experimental conditions. By comparing the numerical simulation with the wind tunnel experimental results, it can be concluded that the aerodynamic force of the airfoil at different angles of attack has good consistency in both numerical and trend aspects, indicating that the experimental scheme is reasonable and feasible.

In addition, the upper and lower walls of the wind tunnel also cause certain disturbances to the CFJ airfoil aerodynamic measurement experiment. Unlike the numerical calculation of the airfoil in a free environment, the wind tunnel's upper and lower walls restrict the fluid's flow, which affects the fluid's flow state and flow field characteristics. In Fig. 20, Simulation 1 represents the pressure distribution of the CFJ airfoil in a free-stream environment, while Simulation 2 represents the pressure distribution in a wind tunnel. The two simulations show little difference in the high-strength low-pressure region at the top of the airfoil. However, in Simulation 2, the low-pressure area with a pressure coefficient of  $-0.25$  or less is confined due to the wall interference, causing the upper wall area of the airfoil to experience low pressure. It generates additional upward lift, causing the positive pressure areas at the leading and trailing edges of the airfoil to move slightly upward and enlarging the positive pressure area. Compared with Simulation 1, the lift coefficient, lift-line slope, drag coefficient, and drag-line slope of the airfoil in Simulation 2 have increased due to the wall interference, and these changes are reflected in the curve variations shown in Figs. 10 and 11. This interference can be

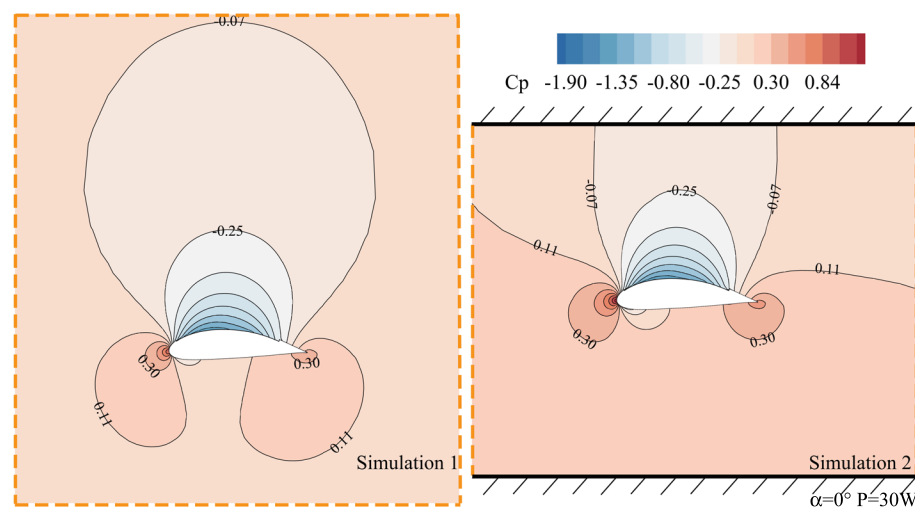


**Fig. 20** Flow field pressure section of the OCFJ airfoil in a free environment (Simulation 1) and a wind tunnel environment (Simulation 2)

reduced by increasing the wind tunnel's size, reducing the airfoil's relative size, or establishing appropriate correction coefficients through experiments and simulations.

## 5 Conclusions

In the present investigation, a meticulously engineered three-stage design methodology was employed to perform aerodynamic evaluations on the CFJ airfoil within a two-dimensional wind tunnel experimental framework. The veracity and practicality of the wind tunnel assessments were corroborated through juxtaposition with CFD simulations. Based on the current work, the following conclusions can be drawn.

1. Dividing the wind tunnel model of the CFJ airfoil into an experimental section and two fixed sections effectively ameliorates the influence of sidewall interference, thereby enhancing the integrity of the aerodynamic measurements.
2. Experimental evidence suggests that as the angle of attack increases, pressure at the leading edge decreases. This decrease allows less energy to be consumed to generate more jets. Subsequently, the co-flow jet's velocity increases, boosting circulation and thus improving aerodynamic efficiency. For instance, when the ducted fan system operates at 30 W, and the angle of attack changes from 0° to 10° with the increments of 2°, experimental measurements indicate that the velocity of the jet flow at the injection nozzle exit increases by 2.30%, 6.76%, 12.08%, 17.66%, and 19.62%, respectively.
3. Co-flow jet technology significantly enhances the aerodynamic performance of the airfoil. As the power level escalates from 10 W to 20 W, the lift coefficient experiences an enhancement of 19.4%, while the drag coefficient undergoes a reduction of 22.6%. Nevertheless, when the power input rises from 20 W to 30 W, the lift and drag coefficients improve by 7.5% and 9.94%, respectively. This trend indicates that although amplifying the power input to the ducted fan system elevates aerodynamic performance, the rate of performance improvement per unit power increment exhibits diminishing returns.

Future research directions encompass the methodological design and analytical evaluation of the co-flow jet wing technology. This includes high-fidelity numerical simulations of CFJ wings under elevated angles of attack for a comprehensive understanding of aerodynamic behaviors. At present, an advanced optimization process is underway, integrating co-flow jet dynamics within the framework of global wing geometry optimization.

### Acknowledgements

We extend our gratitude to the wind tunnel experimental staff at Northwestern Polytechnical University for their assistance in the experiments, and to the editors for their efforts in revising and editing the manuscript.

### Authors' contributions

MX proposed the concept. HJ carried out numerical simulations and experimental simulations. HJ and WY drafted the manuscript. MX and WY reviewed and edited the manuscript, and made the revisions. All authors read and approved the final manuscript.

### Funding

Not applicable.

### Availability of data and materials

The data that support the findings of this study are available from the corresponding author upon reasonable request.

## Declarations

### Competing interests

The authors have no conflicts of interest to disclose.

Received: 1 August 2023 Accepted: 19 October 2023

Published online: 01 December 2023

## References

1. Xu K, Zha G (2023) Enhancing aircraft control surface effectiveness by co-flow jet flap at low energy expenditure. *Aerosp Sci Technol* 133:108145. <https://doi.org/10.1016/j.ast.2023.108145>
2. DeSalvo M, Whalen E, Glezer A (2020) High-lift performance enhancement using active flow control. *AIAA J* 58(10):4228–4242. <https://doi.org/10.2514/1.J059143>
3. Vatsa VN, Lin JC, Melton LP et al (2021) Computational investigation of conventional and active-flow-control-enabled high-lift configurations. *J Aircr* 58(5):1137–1153. <https://doi.org/10.2514/1.C036233>
4. Liu R, Wei W, Wan H et al (2022) Experimental study on airfoil flow separation control via an air-supplement plasma synthetic jet. *Adv Aerodyn* 4:34. <https://doi.org/10.1186/s42774-022-00126-w>
5. Raju R, Mittal R, Cattafesta L (2008) Dynamics of airfoil separation control using zero-net mass-flux forcing. *AIAA J* 46(12):3103–3115. <https://doi.org/10.2514/1.37147>
6. Shi Z, Zhu J, Dai X et al (2019) Aerodynamic characteristics and flight testing of a UAV without control surfaces based on circulation control. *J Aerosp Eng* 32(1):04018134. [https://doi.org/10.1061/\(ASCE\)AS.1943-5525.0000947](https://doi.org/10.1061/(ASCE)AS.1943-5525.0000947)
7. Ye L, Ye Z, Ye K et al (2021) A low-boom and low-drag design method for supersonic aircraft and its applications on airfoils. *Adv Aerodyn* 3:25. <https://doi.org/10.1186/s42774-021-00079-6>
8. Wang W, Liu P, Tian Y et al (2016) Numerical study of the aerodynamic characteristics of high-lift droop nose with the deflection of fowler flap and spoiler. *Aerosp Sci Technol* 48:75–85. <https://doi.org/10.1016/j.ast.2015.10.024>
9. Ramezani A, Chung SJ, Hutchinson S (2017) A biomimetic robotic platform to study flight specializations of bats. *Sci Robot* 2(3):eaal2505. <https://doi.org/10.1126/scirobotics.aal2505>
10. Salcedo MK, Socha JJ (2020) Circulation in insect wings. *Integr Comp Biol* 60(5):1208–1220. <https://doi.org/10.1093/icb/ica124>
11. Zha G, Paxton C (2004) A novel airfoil circulation augment flow control method using co-flow jet. In: 2nd AIAA flow control conference. Portland, 28 June - 1 July 2004. <https://doi.org/10.2514/6.2004-2208>
12. Zha G, Gao W (2006) Analysis of jet effects on co-flow jet airfoil performance with integrated propulsion system. In: 44th AIAA aerospace sciences meeting and exhibit. Reno, 9-12 January 2006. <https://doi.org/10.2514/6.2006-102>
13. Zhang J, Chng TL, Tsai HM (2011) Performance of coflow jet airfoils with conformal slot geometries. *J Aircr* 48(3):1107–1112. <https://doi.org/10.2514/1.C031145>
14. Wang R, Zhang G, Ying P et al (2022) Effects of key parameters on airfoil aerodynamics using co-flow jet active flow control. *Aerospace* 9(11):649. <https://doi.org/10.3390/aerospace9110649>
15. Chng TL, Rachman A, Tsai HM et al (2009) Flow control of an airfoil via injection and suction. *J Aircr* 46(1):291–300. <https://doi.org/10.2514/1.38394>
16. Zha G, Paxton CD, Conley CA et al (2006) Effect of injection slot size on the performance of coflow jet airfoil. *J Aircr* 43(4):987–995. <https://doi.org/10.2514/1.16999>
17. Zha G, Gao W, Paxton CD (2007) Jet effects on coflow jet airfoil performance. *AIAA J* 45(6):1222–1231. <https://doi.org/10.2514/1.23995>
18. Fard MT, He J, Huang H et al (2022) Aircraft distributed electric propulsion technologies-a review. *IEEE Trans Transp Electrification* 8(4):4067–4090. <https://doi.org/10.1109/TTE.2022.3197332>
19. Kaushik M (2019) Potential flow theory. In: Theoretical and experimental aerodynamics. Springer, Singapore, pp 107–126. [https://doi.org/10.1007/978-981-13-1678-4\\_4](https://doi.org/10.1007/978-981-13-1678-4_4)
20. Xu K, Zha G (2022) System energy benefit using co-flow jet active separation control for a serpentine duct. *Aerosp Sci Technol* 128:107746. <https://doi.org/10.1016/j.ast.2022.107746>
21. Dano B, Zha G, Castillo M (2011) Experimental study of co-flow jet airfoil performance enhancement using discrete jets. In: 49th AIAA aerospace sciences meeting including the new horizons forum and aerospace exposition. Orlando, 4-7 January 2011. <https://doi.org/10.2514/6.2011-941>
22. Zhang S, Yang X, Song B et al (2021) Experimental investigation of lift enhancement and drag reduction of discrete co-flow jet rotor airfoil. *Appl Sci* 11(20):9561. <https://doi.org/10.3390/app11209561>
23. Zhang Y, Xu H, Chu Y et al (2021) Two-dimensional numerical study of the pulsed co-flow jet. *Fluid Dyn* 56:361–370. <https://doi.org/10.1134/S0015462821030137>
24. Li B, Meng X, Yin S et al (2022) Flow separation control over an airfoil using plasma co-flow jet. *AIAA J* 60(4):2195–2206. <https://doi.org/10.2514/1.J060911>
25. Lefebvre A, Dano B, Bartow W et al (2016) Performance and energy expenditure of coflow jet airfoil with variation of Mach number. *J Aircr* 53(6):1757–1767. <https://doi.org/10.2514/1.C033113>
26. Wang B, Zha G (2011) Detached-eddy simulation of a coflow jet airfoil at high angle of attack. *J Aircr* 48(5):1495–1502. <https://doi.org/10.2514/1.C000282>
27. Xu K, Zha G (2021) High control authority three-dimensional aircraft control surfaces using coflow jet. *J Aircr* 58(1):72–84. <https://doi.org/10.2514/1.C035727>
28. Xu K, Ren Y, Zha G (2022) Numerical analysis of energy expenditure for coflow wall jet separation control. *AIAA J* 60(5):3267–3285. <https://doi.org/10.2514/1.J061015>
29. Liu J, Chen R, Song Q et al (2022) Active flow control of helicopter rotor based on coflow jet. *Int J Aerosp Eng* 2022:9299470. <https://doi.org/10.1155/2022/9299470>

30. Zhi H, Zhu Z, Lu Y et al (2021) Aerodynamic performance enhancement of co-flow jet airfoil with simple high-lift device. Chin J Aeronaut 34(9):143–155. <https://doi.org/10.1016/j.cja.2021.01.011>
31. Wang R, Ma X, Zhang G et al (2022) Numerical investigation of co-flow jet airfoil with parabolic flap. Chin J Aeronaut 36(5):78–95. <https://doi.org/10.1016/j.cja.2022.08.010>
32. Zhang S, Yang X, Song B (2021) Numerical investigation of performance enhancement of the S809 airfoil and phase VI wind turbine blade using co-flow jet technology. Energies 14(21):6933. <https://doi.org/10.3390/en14216933>
33. Liu J, Chen R, Qiu R et al (2020) Study on dynamic stall control of rotor airfoil based on coflow jet. Int J Aerosp Eng 2020(2020):8845924. <https://doi.org/10.1155/2020/8845924>
34. Jiang H, Xu M, Yao W (2022) Aerodynamic shape optimization of co-flow jet airfoil using a multi-island genetic algorithm. Phys Fluids 34(12):125120. <https://doi.org/10.1063/5.0124372>
35. Hicks RM, Henne PA (1978) Wing design by numerical optimization. J Aircr 15(7):407–412. <https://doi.org/10.2514/3.58379>
36. Zhu M, Yang X, Song C et al (2014) High synergy method for near space propeller using co-flow jet control. Acta Aeronaut Astronaut Sin 35(6):1549–1559. <https://doi.org/10.7527/S1000-6893.2013.0492>
37. Menter FR (1994) Two-equation eddy-viscosity turbulence models for engineering applications. AIAA J 32(8):1598–1605. <https://doi.org/10.2514/3.12149>

## Publisher's Note

Springer Nature remains neutral with regard to jurisdictional claims in published maps and institutional affiliations.

Submit your manuscript to a SpringerOpen® journal and benefit from:

- Convenient online submission
- Rigorous peer review
- Open access: articles freely available online
- High visibility within the field
- Retaining the copyright to your article

Submit your next manuscript at ► [springeropen.com](http://springeropen.com)